PNAS RESEARCH ARTICLE | CELL BIOLOGY
BIOPHYSICS AND COMPUTATIONAL BIOLOGY

The endoplasmic reticulum adopts two distinct tubule forms

Bowen Wang[a,b,c], Zhiheng Zhao[a,b,c], Michael Xiong[a,b,c], Rui Yan[a,b,c], and Ke Xu[a,b,c,1]

Edited by Jodi Nunnari, University of California, Davis, CA; received October 27, 2021; accepted March 3, 2022

The endoplasmic reticulum (ER) is a versatile organelle with diverse functions. Through superresolution microscopy, we show that the peripheral ER in the mammalian cell adopts two distinct forms of tubules. Whereas an ultrathin form, R1, is consistently covered by ER-membrane curvature-promoting proteins, for example, Rtn4 in the native cell, in the second form, R2, Rtn4 and analogs are arranged into two parallel lines at a conserved separation of ∼105 nm over long ranges. The two tubule forms together account for ∼90% of the total tubule length in the cell, with either one being dominant in different cell types. The R1–R2 dichotomy and the final tubule geometry are both coregulated by Rtn4 (and analogs) and the ER sheet–maintaining protein Climp63, which, respectively, define the edge curvature and lumen height of the R2 tubules to generate a ribbon-like structure of well-defined width. Accordingly, the R2 tubule width correlates positively with the Climp63 intraluminal size. The R1 and R2 tubules undergo active remodeling at the second/subsecond timescales as they differently accommodate proteins, with the former effectively excluding ER-luminal proteins and ER-membrane proteins with large intraluminal domains. We thus uncover a dynamic structural dichotomy for ER tubules with intriguing functional implications.

ER tubules | organelle morphology | superresolution microscopy | ER-shaping proteins | endoplasmic reticulum

Significance

The endoplasmic reticulum (ER) is one of the most structurally visible and functionally important organelles in the cell. Utilizing superresolution microscopy, we here unveil that in the mammalian cell, the peripheral ER adopts two distinct, well-defined tubule forms of contrasting structures, molecular signatures, and functions, with one of the two curiously being ribbon-like, ultranarrow sheets of fixed widths. With fast multicolor microscopy, we further show how the two tubule forms dynamically interconvert while differentially accommodating proteins in the living cell.

Being the largest and most expansive organelle in the cell, the endoplasmic reticulum (ER) carries diverse key functions from protein and lipid synthesis, protein folding and modification, transport, and calcium storage, to organelle interactions (1–6). The shaping mechanism of this complex, membrane-bounded organelle is thus of fundamental significance (7–21).

The fully connected ER system is classically subdivided into three distinct domains, namely the nuclear envelope, ER sheets, and ER tubules. The latter two structures, collectively known as the "peripheral ER," interweave into a dynamic, interconvertible network, yet are differently maintained and regulated by ER-shaping proteins. In mammalian cells, the two-dimensional ER sheets consist of two flat lipid bilayers at an ∼50-nm separation (3, 4, 11); this conserved luminal spacing is maintained by Climp63 (CKAP4), a transmembrane protein that forms intraluminal bridges between the opposing membranes via its extended coiled-coil domain (11, 20, 22). Meanwhile, the highly curved edges of the ER sheets are stabilized by curvature-promoting proteins including the reticulons (Rtns) and REEPs (8, 11), which, with their hairpin-like topology, insert into the outer leaflet of the lipid bilayer as wedges (9, 10, 12, 21). The same curvature-promoting proteins also stabilize the high curvatures in the one-dimensional ER tubules (9, 10), which in mammalian cells are often taken as cylindrical tubules of ∼50- to 100-nm diameter (2, 7). Notably, the intracellular overexpression of the reticulon Rtn4 (Nogo) substantially reduces the ER-tubule diameter to ∼20 nm, highlighting its ability to shape high-curvature tubules (10).

The rise of superresolution microscopy (SRM) over the past decade offers new means to discover cellular structures (23–25). When applied to the ER (14, 17–19, 26, 27), new perspectives have emerged to challenge the traditional division between ER sheets and tubules, for example, whether the peripheral ER sheets should be viewed as a matrix of tubules or sheets with many nanoscale holes (17, 19). Here, we instead focus on the ER tubules and, unexpectedly, suggest that a substantial fraction of the ER tubules should be recognized as thinned and elongated sheets of fixed widths defined by Climp63–Rtn interactions.

Results

Stochastic Optical Reconstruction Microscopy Unveils an ER-Tubule Dichotomy. We started by applying stochastic optical reconstruction microscopy (STORM) SRM (28, 29), which routinely achieves ∼20-nm spatial resolution, to immunolabeled endogenous Rtn4 in untransfected COS-7 cells. Rtn4 is one of the most studied

Author affiliations: [a]Department of Chemistry, University of California, Berkeley, CA 94720; [b]California Institute for Quantitative Biosciences, University of California, Berkeley, CA 94720; and [c]Chan Zuckerberg Biohub, San Francisco, CA 94158

Author contributions: B.W., R.Y., and K.X. designed research; B.W., Z.Z., and M.X. performed research; B.W. and R.Y. contributed new reagents/analytic tools; B.W., Z.Z., M.X., and K.X. analyzed data; and B.W. and K.X. wrote the paper.

The authors declare no competing interest.

This article is a PNAS Direct Submission.

[1]To whom correspondence may be addressed. Email: xuk@berkeley.edu.

This article contains supporting information online at http://www.pnas.org/lookup/suppl/doi:10.1073/pnas.2117559119/-/DCSupplemental.

Published April 26, 2022.

ER-membrane curvature-promoting proteins in the mammalian cell, and quantitative proteomics of a human cell line has indicated it as the most abundant member of the group (30). Similar results were obtained using two different antibodies (*SI Appendix*, Fig. S1), and immunoblotting indicated that Rtn4b and Rtn4b2 were the dominant Rtn4 forms detected in our experiments (*SI Appendix*, Fig. S2).

Unexpectedly, we found that in a major fraction of the ER tubules, Rtn4 showed up as two parallel lines over long ranges (filled arrowheads in Fig. 1 *A* and *B*). The typical center-to-center distance between the two lines was ∼105 nm (Fig. 1*C*), and statistics showed a conserved narrow distribution of 106 ± 18 nm between different cell types (Fig. 1*D*). This well-defined separation suggests a distinct structural arrangement and hence classification, which we hereby designate as R2 (Rtn double-line).

Meanwhile, we also observed a second class of ER tubules in which Rtn4 appeared as a thin single line (henceforth R1) of ∼50-nm FWHM (full width at half maximum) (Fig. 1*E*). In COS-7 cells, they existed as short segments connecting the R2 tubules (hollow arrowheads in Fig. 1*A*), but also as longer tubules, often at the cell periphery, as the extremities of the ER network (hollow arrowheads in Fig. 1*B*). Together, ∼75 and ∼15% of the total ER-tubule lengths in COS-7 cells were classified as the R2 and R1 forms, respectively, with the remaining ∼10% being ambiguous (Fig. 1*F*). Thus, STORM unveiled an R1–R2 dichotomy of ER tubules, with R2 being the dominating form in COS-7 cells.

As we next examined seven other cell types, we found two epithelial cell lines, BS-C-1 (Fig. 1*G*) and U2OS (Fig. 1*H*), similarly exhibited an R2-dominant R1–R2 dichotomy (Fig. 1*F*). In contrast, two fibroblast cell lines (A7r5 and NIH 3T3; Fig. 1 *J* and *K*) and a myoblast cell line (C2C12; Fig. 1*L*) had >75% of the ER tubules in the R1 form and ∼10% in the R2 form as sporadic, short segments (filled arrowheads in Fig. 1 *J*–*L*). A drastic contrast was further noted between the cultured primary astrocytes and neurons from rat hippocampus: Whereas in the astrocytes the ER tubules were predominantly (∼80%) R2, and this form was maintained along the thin,

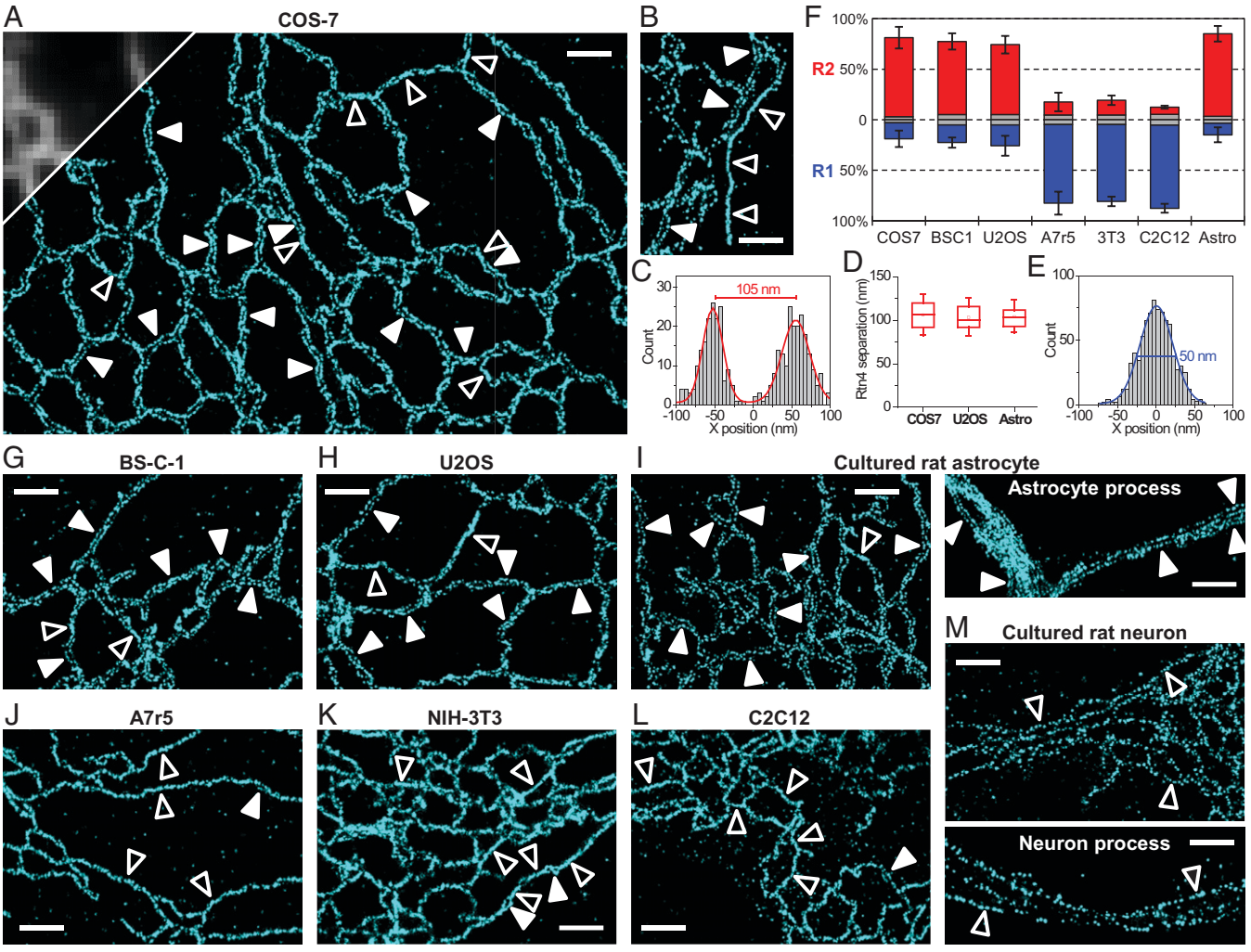

Fig. 1. STORM SRM of endogenous Rtn4 unveils a structural dichotomy for ER tubules. (*A*) Representative STORM image of immunolabeled Rtn4 in the untransfected COS-7 cell, compared with a diffraction-limited fluorescence image (*Upper Left*). Filled and hollow arrowheads point to examples of R2 (Rtn double-line) and R1 (Rtn single-line) tubules, respectively. (*B*) Result from another COS-7 cell, highlighting a long R1 tubule at the extremity of the ER network. (*C*) Representative STORM image intensity (as single-molecule counts) across an R2 tubule. (*D*) Distribution of the STORM-determined center-to-center separations between opposing Rtn4 lines in the R2 tubules in the native COS-7 cells, U2OS cells, and cultured rat astrocytes. Whiskers and boxes show 10, 25, 50, 75, and 90% quantiles. For each data point, $n = 200$ local distances were pooled from five cells. (*E*) Representative STORM image intensity across an R1 tubule. Blue curve: fit to a Gaussian distribution of 50-nm FWHM. (*F*) The fractions of R1 and R2 tubules by length, observed in different cell types. Blue, R1; red, R2; gray, ambiguous. Error bars indicate SDs between $n = 5$ cells of each type. (*G*–*M*) Representative STORM images of immunolabeled endogenous Rtn4 in different cell lines: BS-C-1 (monkey epithelial; *G*), U2OS (human epithelial; *H*), A7r5 (rat fibroblast; *J*), NIH 3T3 (mouse fibroblast; *K*), and C2C12 (mouse myoblast; *L*), as well as in cultured primary astrocytes (*I*) and neurons (*M*) from rat hippocampus. (Scale bars, 1 μm.)

elongated processes (Fig. 1*I*), most ER tubules in the neurons appeared R1 (Fig. 1*M*).

Regulation of the R1–R2 Dichotomy. Our unexpected observation of two distinct ER-tubule forms begs structural explanations. For the R1 tubules, the STORM-measured ∼50-nm apparent FWHM is comparable to that found (51 nm) for the ∼25-nm-diameter microtubules under similar experimental conditions (29) given the antibody sizes and localization precisions. To simplify the discussion and consider the ∼4-nm lipid-bilayer thickness, we take the outer, inner (luminal), and mean diameters of the R1 tubule as 24, 16, and 20 nm, respectively. These very small diameters and hence high membrane curvatures may be maintained by a consistent coverage of the curvature-promoting Rtn4 along the circumference. Indeed, as we overexpressed Rtn4b-GFP (green fluorescent protein) in the R2-dominating COS-7 cells, STORM showed that accompanying the reduction of ER sheets and enhanced presence of ER tubules (9), ∼90% of the ER tubules turned into the ultrathin R1 form (Fig. 2 *B*, *C*, and *F* and *SI Appendix*, Fig. S3), in stark contrast to the ∼75% R2 fraction in the untransfected cells (Fig. 1 *A* and *F*). Nonetheless, sporadic R2 segments were infrequently spotted along the predominantly R1 tubules (filled arrowhead in Fig. 2*C*), and we occasionally observed cells that retained >10% R2 tubules (*SI Appendix*, Fig. S3), suggesting that the R1–R2 dichotomy is still the preferred configuration under Rtn4 overexpression.

For the R2 tubules, the restriction of Rtn4 to two parallel lines raises a possibility that here Rtn4 stabilizes the edges of elongated, ribbon-like ER sheets (or compressed tubes) with two highly curved sides but relatively flat tops and bottoms (Fig. 2*A*; see also *SI Appendix*, Fig. S4 for electron microscopy of ER-tubule cross-sections). If that were the case, ER sheet–maintaining proteins such as Climp63 would likely regulate the luminal height of the R2 tubules as in typical ER sheets (11, 20). Indeed, fluorescence microscopy has shown the presence of Climp63 in ER tubules (11, 17, 18, 31), and a recent SRM study discusses the possible roles of Climp63 in regulating luminal compartmentalization and heterogeneity as "nanodomains" (18). Two-color STORM showed that whereas Climp63 and Rtn4, respectively, filled the ER sheets and delineated the sheet edges (asterisks in Fig. 2*D* and *SI Appendix*, Fig. S5), as expected, a relatable structural arrangement further extended into the R2 tubules (filled arrowheads in Fig. 2 *D* and *E*). In contrast, the R1 tubules were devoid of Climp63 (hollow arrowheads in Fig. 2 *D* and *E*).

In COS-7 cells, the overexpression of Climp63 led to the expansion of ER sheets and the reduction of ER tubules (*SI Appendix*, Fig. S5), consistent with previous reports (11). Meanwhile, STORM showed that the ER tubules remained predominantly (∼80%) R2 (*SI Appendix*, Fig. S5). Conversely, Climp63 small interfering RNA (siRNA) markedly reduced R2 tubules to ∼30%, albeit with large cell-to-cell variations (Fig. 2*F* and *SI Appendix*, Fig. S6), potentially due to inhomogeneous knockdown levels and/or the existence of other ER-luminal spacer proteins. In the R1-dominating NIH 3T3 cells, overexpressed Climp63 entered a significant fraction of the ER tubules to produce the R2 form (*SI Appendix*, Fig. S7). However, in some cells, Climp63 was highly localized to ER sheets and hardly entered the tubules, for which cases the ER tubules remained dominantly R1 (*SI Appendix*, Fig. S7). Together, our results suggest Rtn4 and Climp63 coregulate the R1–R2 dichotomy: High Rtn4 levels promote R1 tubules, whereas the entering of Climp63 into tubules produces the R2 form.

Defining the R2 Tubule Width. To rationalize the remarkably conserved ∼105-nm distance between the opposing Rtn4 lines in the R2 tubules, we consider a simple model in which Climp63 sets the R2 tubule height h to the typical lumen height of ER sheets (∼50 nm) (11, 20), whereas Rtn4 holds the membrane radius of curvature at the two edges at some preferred value of r_e. To a first approximation, we assume that the tubule adopts a smooth, elliptical cross-section. The ellipse geometry yields $r_e = h^2/2w$, where w ∼100 nm is the ellipse width (∼105-nm Rtn4–Rtn4 separation minus the lipid-bilayer thickness). With h ∼50 nm, r_e is thus estimated as ∼12.5 nm, slightly larger than the assumed ∼10-nm radius of curvature of

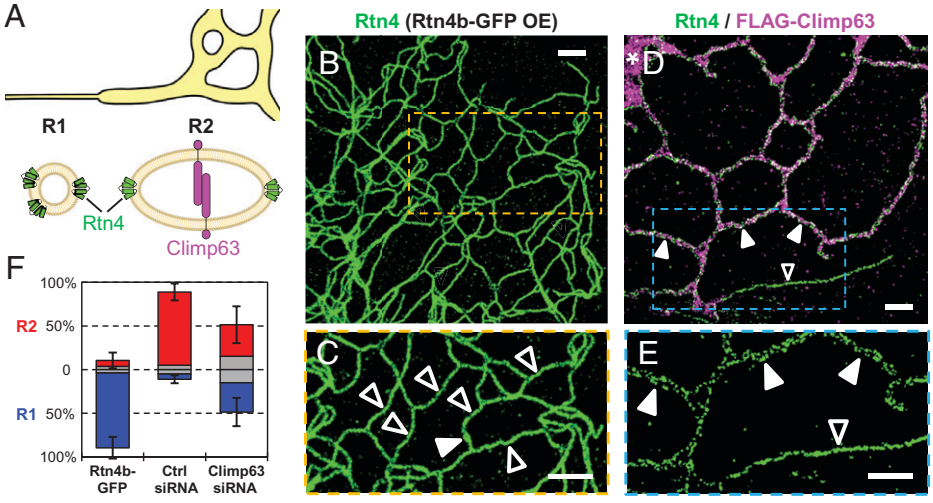

Fig. 2. Rtn4 and Climp63 coregulate the R1–R2 dichotomy. (*A*) Model. In the R1 tubules, high membrane curvatures are stabilized by a consistent Rtn4 coverage. In the R2 tubules, Rtn4 stabilizes the two highly curved edges of ribbon-like ER sheets, whereas Climp63 defines the luminal height. (*B*) Representative STORM image of immunolabeled Rtn4 in a COS-7 cell overexpressing Rtn4b-GFP. OE, overexpression. (*C*) Close-up of the box in *B*. (*D*) Representative two-color STORM image of the immunolabeled endogenous Rtn4 (green) and overexpressed FLAG-Climp63 (magenta) in a COS-7 cell. The asterisk indicates an ER sheet. (*E*) Close-up of the Rtn4 channel of the box in *D*. Filled and hollow arrowheads point to examples of R2 and R1 tubules, respectively. (*F*) The fractions of R1 and R2 tubules by length, observed in COS-7 cells overexpressing Rtn4b-GFP or treated with control siRNA or Climp63 siRNA. Blue, R1; red, R2; gray, ambiguous. Error bars indicate SDs between $n = 6$ cells for each condition. (Scale bars, 1 μm.)

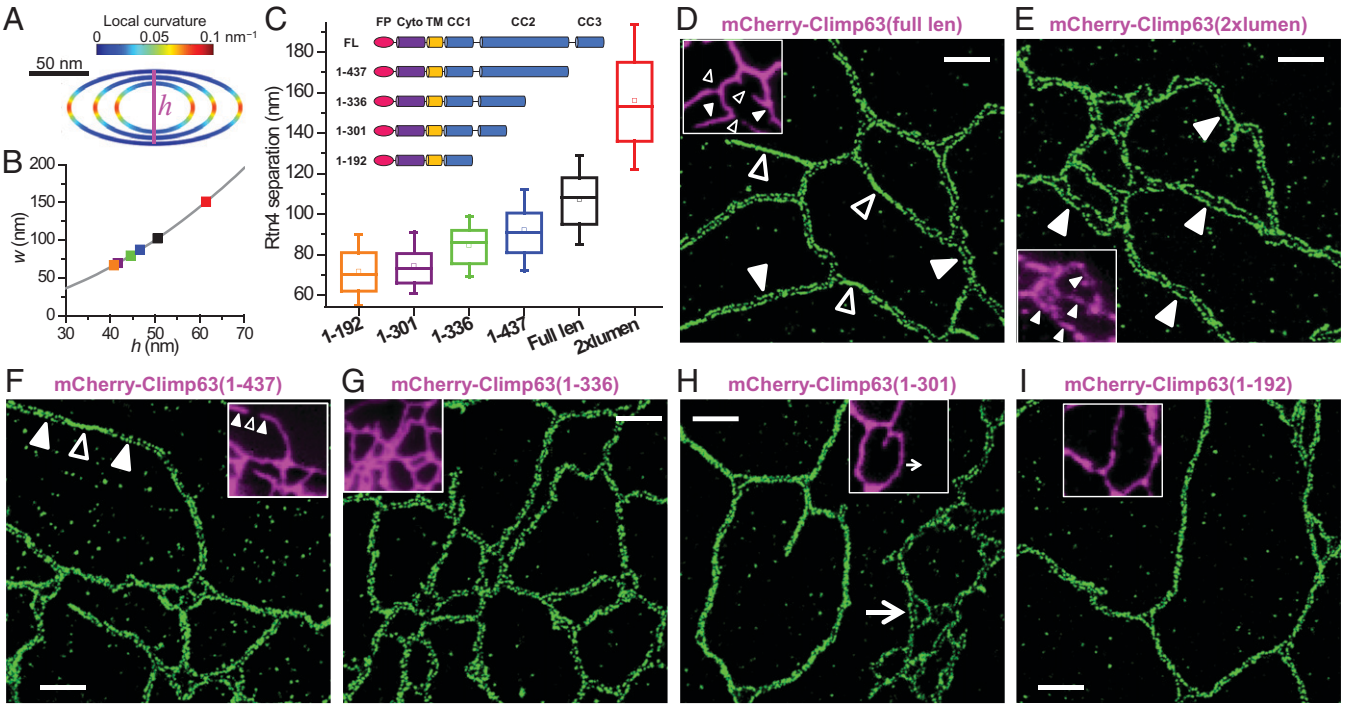

Fig. 3. Rtn4 and Climp63 jointly define the R2 tubule width. (*A*) A simple model of the R2 tubule based on an elliptical cross-section, in which the luminal height h is varied as the membrane curvature at the two edges is held at $1/r_e = 0.08$ nm^{-1}. Color represents the local curvature. (*B*) The expected R2 tubule width w as a function of h according to this simple model (line). Colored squares mark the experimental w for cells expressing the different Climp63 mutants in *C*, calculated as the STORM-determined Rtn4–Rtn4 separations minus 5-nm lipid-bilayer thickness. (*C*) Distribution of center-to-center separations between opposing Rtn4 lines in R2 tubules, for COS-7 cells expressing mCherry-tagged mouse Climp63 mutants of different intraluminal sizes. Whiskers and boxes show 10, 25, 50, 75, and 90% quantiles. For each data point, $n = 200$ local distances were pooled from five cells. (*C*, *Inset*) Schematics of the full-length (FL) and truncated Climp63 versions examined. CC1 to CC3, intraluminal coiled-coil domains; Cyto, cytosolic domain; FP, mCherry fluorescent protein; TM, transmembrane domain. (*D*–*I*) Representative STORM images of the immunolabeled endogenous Rtn4 in COS-7 cells expressing mCherry-tagged full-length (1–575) (*D*), 2xlumen (*E*), 1–437 (*F*), 1–336 (*G*), 1–301 (*H*), and 1–192 (*I*) mutants of mouse Climp63. (*D*–*I*, *Insets*) Epifluorescence images of the mCherry channel. Filled and hollow arrowheads point to examples of R2 and R1 tubules, respectively. In *H*, the arrow points to an untransfected cell in the same view, which facilitates a direct comparison. (Scale bars, 1 μm.)

the ultrathin R1 tubules above, yet slightly smaller than the ∼15-nm value used in previous models for ER-sheet edges (11).

Under the above simple model of fixed curvatures at the two vertices of an elliptical cross-section, the R2 tubule width $w \sim h^2/2r_e$ would correlate positively with the lumen height h (Fig. 3 *A* and *B*). Recent experiments have shown that for ER sheets, h can be altered by varying the length of the intraluminal coiled-coil domain of Climp63 (20). We utilized this strategy and STORM-imaged Rtn4 in COS-7 cells expressing different mCherry-tagged Climp63 variants. Expression of the full-length mouse Climp63(1–575) reaffirmed the respective presence and absence of Climp63 in the R2 and R1 tubules (Fig. 3*D*), with the STORM-determined Rtn4–Rtn4 separation in the former unchanged (107 ± 17 nm; Fig. 3*C*). In contrast, the expression of a mutant that doubled the intraluminal domain, Climp63(2xlumen), which may raise h to ∼70 nm (20), substantially increased the Rtn4–Rtn4 separation in R2 tubules to ∼155 nm (Fig. 3 *C* and *E*). Conversely, the expression of mouse Climp63 mutants with truncated intraluminal domains (22), namely Climp63(1–437) with the removal of the third coiled-coil domain and Climp63(1–336), Climp63(1–301), and Climp63(1–192) with further partial and complete removals of the second coiled-coil domain (see schematics in Fig. 3 *C*, *Inset*), led to progressive reductions of the Rtn4–Rtn4 separation (Fig. 3 *C* and *F*–*I*). In the limit of the shortest version, for which h ∼30 nm may be expected (20), this value reduced to ∼70 nm (Fig. 3 *C* and *I*), although the very small separations made quantification difficult. As we again subtracted 5 nm for the lipid-bilayer thickness, the resultant w values corresponded to h ∼41 to 62 nm with our simple model (Fig. 3*B*). This range is smaller than previously measured for ER sheets with comparable Climp63 variants (h ∼30 to 70 nm) (20), which may be reconciled by relaxing the primitive assumptions in our model of fixed edge curvatures and the simple ellipse geometry. Together, our results suggest that Climp63 and Rtn4 jointly define the R2 tubule width.

The R1 and R2 Tubules Differentially Accommodate ER Proteins. The above contrasting structures of R1 and R2 tubules may differentially regulate the distributions of ER proteins. With R1 tubules of ∼16-nm luminal diameter and R2 tubules of elliptical width and height of ∼100 and ∼50 nm, the luminal cross-sectional areas of the two tubule types differ by ∼20-fold. Further considering the protein exclusion volume, for a protein 5 nm in size, the accessible luminal volume per unit length is ∼35-fold different between the two tubule types. Indeed, two-color STORM of immunolabeled Rtn4 versus the endogenous calreticulin (Fig. 4*A*) and the expressed ER-residing fluorescent protein mEmerald-ER-3 (Fig. 4*B*) showed that both ER-luminal proteins were abundant in the R2 tubules (filled arrowheads) but absent from the R1 tubules (hollow arrowheads). Our model also predicts an ∼4-fold difference in the cross-sectional circumference, and hence the membrane surface area per unit length, between the R2 and R1 tubules. Accordingly, two-color STORM showed reduced, yet not eliminated, presence of overexpressed sec61b, a common ER-membrane marker, in the R1 tubules when compared with the R2 tubules

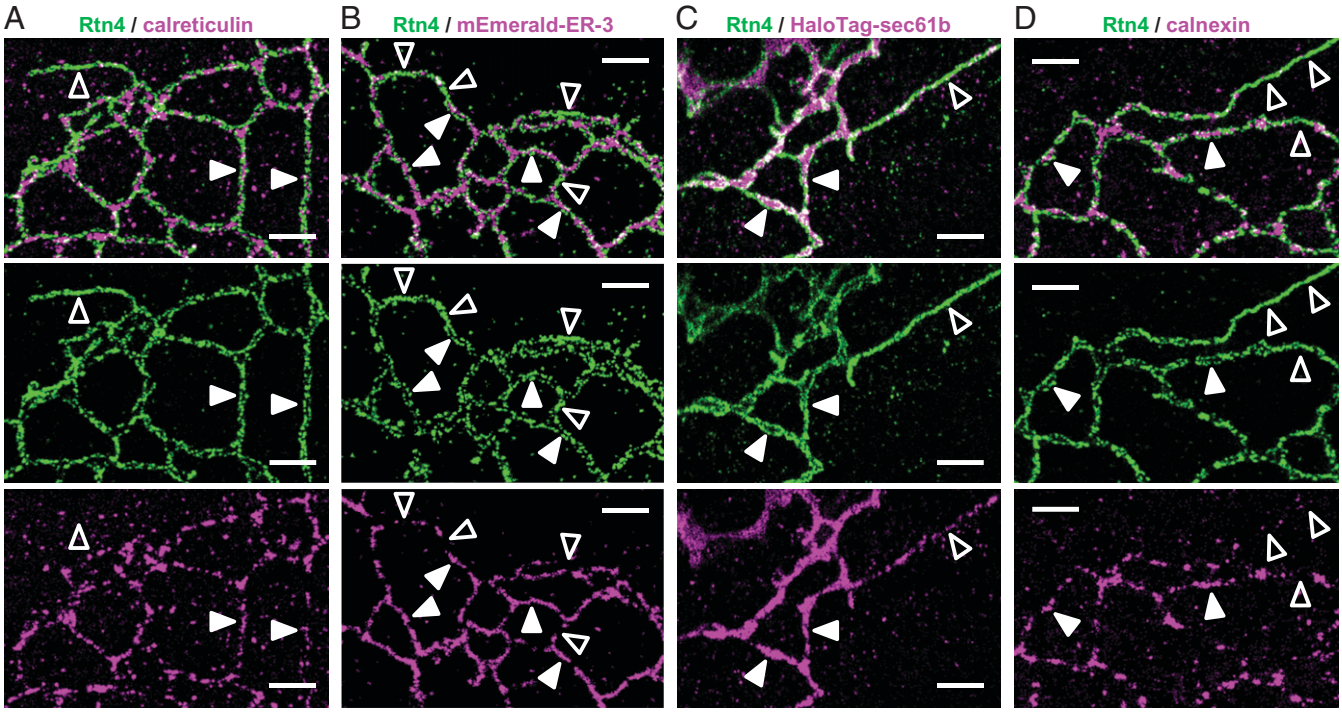

Fig. 4. R1 and R2 tubules differentially accommodate ER proteins. (*A*) Representative two-color STORM image of the immunolabeled endogenous Rtn4 (green) and calreticulin (magenta) in an untransfected COS-7 cell. (*B* and *C*) Representative two-color STORM images of the immunolabeled endogenous Rtn4 (green) and expressed ER-luminal protein mEmerald-ER-3 (magenta in *B*) and ER-membrane protein HaloTag-sec61b (magenta in *C*) in COS-7 cells. (*D*) Representative two-color STORM image of the immunolabeled endogenous Rtn4 (green) and calnexin (magenta) in an untransfected COS-7 cell. Filled and hollow arrowheads point to examples of R2 and R1 tubules, respectively. (Scale bars, 1 μm.)

(Fig. 4*C*). Interestingly, we next found that calnexin, an ER-transmembrane protein with a large intraluminal domain (32), was largely excluded from the R1 tubules (Fig. 4*D*). To examine the role of the intraluminal domain, we expressed in COS-7 cells two constructs with the transmembrane domain of calnexin (canxTM) linked to the 27-kDa GFP mEmerald at the intraluminal and extraluminal (cytosolic) sides, respectively. Two-color STORM with Rtn4 showed that the former was more excluded from the R1 tubules than the latter (*SI Appendix*, Fig. S8). Together, our results suggest that intraluminal crowding prevents both ER-luminal proteins and ER-membrane proteins with large intraluminal domains from entering the R1 tubules. The dynamics of this regulating mechanism is further examined below with live-cell experiments.

R1–R2 Dynamics in Live Cells. To probe the R1–R2 tubule dynamics in live cells, we coexpressed Rtn4b-GFP and mCherry-Climp63 in COS-7 cells. Although the single overexpression of Rtn4 and Climp63, respectively, biased ER tubules toward R1 and R2 (Fig. 2 *B*, *C*, and *F* and *SI Appendix*, Figs. S3 and S7), we reasoned that the coexpression of both proteins may counterbalance the two tubule forms. Previous work has noted normal ER morphologies in cells cooverexpressing Rtn4 and Climp63 (11). We observed a mixed population of both mCherry-Climp63–positive and –negative ER-tubule segments (filled and open arrowheads in Fig. 5*A*). Correlating the same view with STORM of immunolabeled Rtn4 (Fig. 5*B* and *SI Appendix*, Fig. S9) showed that the two segment forms scrupulously corresponded to R2 and R1, respectively, consistent with our above model that the entering of Climp63 into tubules produces the R2 form. Thus, by tracking in the wide-field micrographs which tubule segments were Climp63-positive, we followed the R1–R2 tubule dynamics in live cells at high temporal resolutions.

Both the R1 and R2 tubules were highly dynamic, with extensive restructuring constantly occurring at the second/subsecond timescales (Movies S1–S4). For the fast-extending ER tubules, we found that the outgrowing tips were often in the Climp63-free R1 form (o1 in Fig. 5*C*; see also *SI Appendix*, Fig. S10 and Movies S1 and S2). Climp63 then gradually extended into the tubules to establish the R2 form and, interestingly, may do so in consecutive segments (e1 to e3 in Fig. 5*C*; see also *SI Appendix*, Fig. S10).

A trove of intriguing R1–R2 dynamics was further observed in the tubule networks (Fig. 5 *D* and *E*; see also *SI Appendix*, Figs. S10 and S11 and Movies S2–S4). Besides the above-noted R1-led tubule outgrowth (o1 to o4 in Fig. 5*E* and *SI Appendix*, Fig. S11) and the extension of Climp63 into R1 tubules (e1 to e4 in Fig. 5*E*), we often observed the splitting of Climp63-positive R2 tubules into multiple R2 segments connected by Climp63-free R1 segments (s1 and s2 in Fig. 5*E*), the fusion between R2 segments (f1 and f2 in Fig. 5*E*), the translational motion of R2 segments (t1 and t2 in Fig. 5*E*), the entering of R2 segments into new branches (b1 to b3 in Fig. 5*E*), and the fast withdrawal of newly extended tubules (w1 and w2 in Fig. 5*E*).

Three-color live-cell imaging next showed that the ER-luminal protein HaloTag-ER-3 stayed exclusively in the R2 tubules (filled arrowheads in Fig. 5*F*) and so cotraveled with the Climp63-positive segments throughout the R1–R2 rearrangements (Fig. 5 *G* and *H* and Movie S5). In contrast, the ER-membrane protein mEmerald-sec61b exhibited a reduced, yet still substantial, presence in the R1 tubules (hollow arrowheads in Fig. 5*I*), and this distribution was also preserved as the R1–R2 tubules dynamically rearranged in the cell (Fig. 5 *J* and *K* and Movie S6). Comparison with STORM results on fixed cells reaffirmed the above observations (*SI Appendix*, Fig. S12). Thus, consistent with our two-color STORM results above

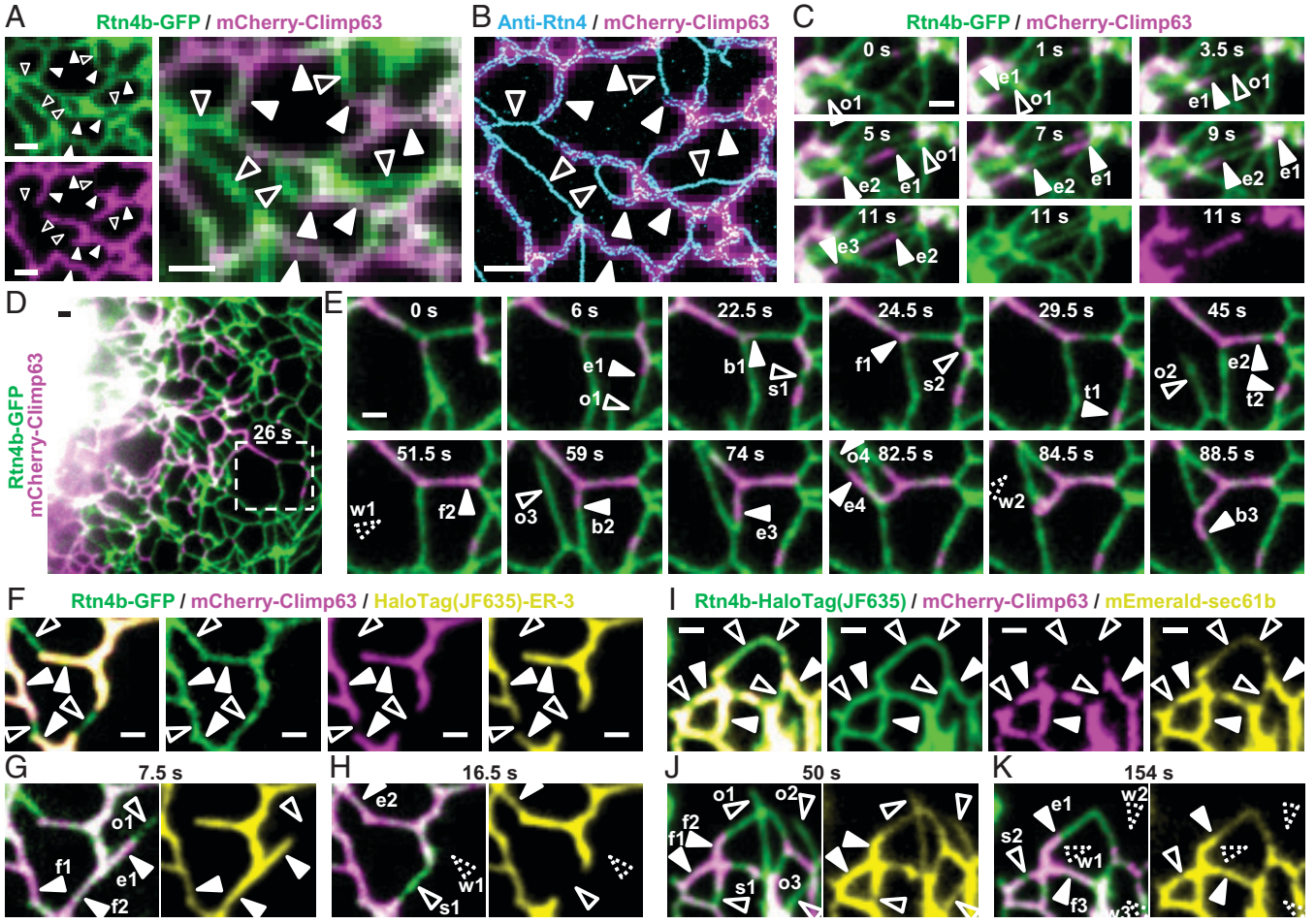

Fig. 5. Live-cell imaging unveils fast R1–R2 remodeling and associated cotraveling of ER proteins. (*A*) Two-color fluorescence micrographs of Rtn4b-GFP (green) and mCherry-Climp63 (magenta) coexpressed in a COS-7 cell, shown as separate channels (*Left*) and an overlay (*Right*). (*B*) STORM of immunolabeled Rtn4 of the same view (cyan), overlayed with the mCherry-Climp63 micrograph (magenta). Filled and hollow arrowheads point to R2 and R1 examples, respectively. (*C*) Two-color micrographs of Rtn4b-GFP (green) and mCherry-Climp63 (magenta) for a small region in a living COS-7 cell at selected time points, highlighting ER-tubule outgrowth with a Climp63-free R1 tip (o1) and the ensuing extension of Climp63 into the tubule in segments (e1 to e3). The two separated color channels are shown for the final image. See also separated color channels in *SI Appendix*, Fig. S10 and a full series in Movie S1. (*D*) Another two-color live-cell dataset. (*E*) Selected time points for the boxed region in *D*. Arrowheads point to major structural changes vs. the preceding image. o1 to o4: tubule outgrowths with Climp63-free R1 tips; e1 to e4: extension of Climp63 into R1 tubules; s1 to s2: the sequential splitting of a Climp63-positive R2 segment into three R2 segments connected by Climp63-negative R1 segments; f1 and f2: fusion of an R2 tubule with two small R2 segments; t1 and t2: translational motions of two R2 segments along tubules; b1 to b3: Climp63 entering new tubule branches; w1 and w2: withdrawal of newly extended tubules. See separated color channels in *SI Appendix*, Fig. S11 and a full series in Movies S3 and S4. (*F*) Live-cell three-color imaging of Rtn4b-GFP (green), mCherry-Climp63 (magenta), and JF635-labeled HaloTag-ER-3 (yellow) in a COS-7 cell, shown as merged and separated channels. (*G* and *H*) The same region after 7.5 s (*G*) and 16.5 s (*H*), shown as merged Rtn4b-GFP/mCherry-Climp63 (*Left*) and HaloTag-ER-3 alone (*Right*). See the full series in Movie S5. (*I*) Live-cell three-color imaging of JF635-labeled Rtn4b-HaloTag (green), mCherry-Climp63 (magenta), and mEmerald-sec61b (yellow) in a COS-7 cell, shown as merged and separated channels. (*J* and *K*) The same region after 50 s (*J*) and 154 s (*K*), shown as merged Rtn4b-HaloTag/mCherry-Climp63 (*Left*) and mEmerald-sec61b alone (*Right*). See the full series in Movie S6. Filled and hollow arrowheads in *F* and *I* point to R2 and R1 examples, respectively. Arrowheads in *G*, *H*, *J*, and *K* point to major structural changes annotated similar to *E*. (Scale bars, 1 μm.)

(Fig. 4), the R1 tubules excluded ER-luminal proteins but accommodated low levels of ER-membrane proteins during the fast R1–R2 remodeling.

The R1–R2 Dichotomy Also Applies to Other ER-Membrane Curvature Proteins. Our above results with the ubiquitously abundant Rtn4 prompt the question of whether other ER-membrane curvature-promoting proteins may behave similarly. To address this question, we expressed in COS-7 cells GFP-tagged Rtn4b, Rtn3c, REEP5 (DP1), and Arl6IP1. STORM through immunostaining with an anti-GFP antibody tagged with Alexa Fluor 647 showed that when overexpressed individually, all four proteins consistently covered the ER tubules in the ultrathin R1 form, with short R2 segments only sporadically spotted (Fig. 6*A*). These results are similar to what we observed above with STORM of anti-Rtn4 when overexpressing Rtn4b (Fig. 2 *B* and *C* and *SI Appendix*, Fig. S3). When coexpressed with mCherry-Climp63, STORM of anti-GFP further showed R1–R2 dichotomies for all four proteins, so that they showed up as two parallel lines for the Climp63-positive tubule segments (filled arrowheads in Fig. 6*B*) but remained in the R1 form for segments devoid of Climp63 (hollow arrowheads in Fig. 6*B*), again mimicking the above behavior of Rtn4 (Fig. 5*B*). These observations suggest that the R1–R2 dichotomy is a general structural arrangement for ER tubules. Different curvature-preferring membrane proteins may thus work together to both promote/stabilize the ultrathin R1 tubules and cooperate with Climp63 to stabilize the two high-curvature edges of the ribbon-like R2 tubules.

Discussion

Together, our superresolution and live-cell microscopy results introduced an R1–R2 dichotomy for ER tubules and unveiled

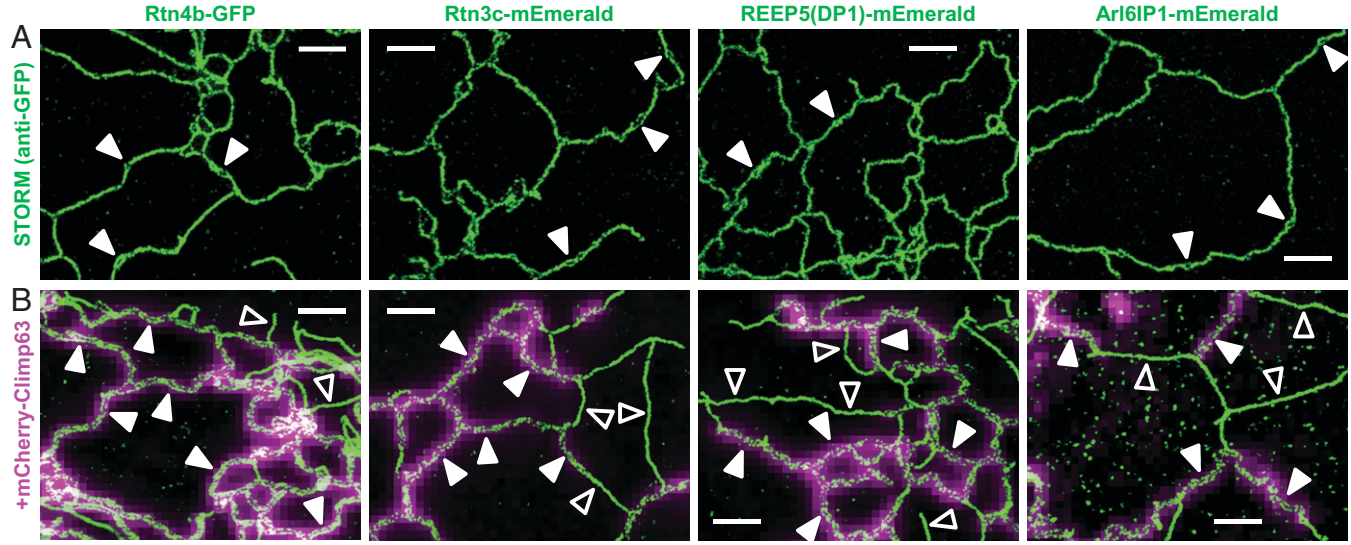

Fig. 6. R1–R2 dichotomy also applies to other ER-membrane curvature proteins. (*A*) Representative STORM images of Rtn4b-GFP, Rtn3c-mEmerald, REEP5 (DP1)-mEmerald, and Arl6IP1-mEmerald expressed in COS-7 cells. STORM was performed after immunostaining with an anti-GFP antibody tagged with Alexa Fluor 647. Filled arrowheads point to small R2 segments, whereas most other tubules appear as R1. (*B*) Representative STORM images of Rtn4b-GFP, Rtn3c-mEmerald, REEP5 (DP1)-mEmerald, and Arl6IP1-mEmerald (green) overlaid with epifluorescence images of mCherry-Climp63 (magenta) coexpressed in the same COS-7 cells. Filled and hollow arrowheads point to R2 and R1 examples, respectively. (Scale bars, 1 μm.)

their dynamics and functional implications. Though our R1–R2 model is unexpected, it explains and connects several recent findings.

Live-cell STORM experiments with a membrane dye have noted that in BS-C-1 cells, the newly extended ER tubules are substantially thinner (26). However, the origin of this phenomenon has not been elucidated. We showed that the extending "new" tubule tips were often of the thinner R1 form, yet the established "old" tubule networks were also characterized by dynamic R1–R2 rearrangements. Meanwhile, electron microscopy (EM) has visualized ∼20 nm–sized "ultrathin" ER tubules in COS cells upon Rtn4 overexpression (10). Fluorescence microscopy notes that the overexpression of Rtn4, Rtn3c, REEP5 (DP1), Arl6IP1, and like proteins tend to "squeeze out" luminal proteins from the ER tubules (10, 12, 33–35). These observations may be understood under our R1–R2 framework as that raised levels of curvature-promoting proteins drive ER tubules into the luminal protein–excluding R1 form. Yet, our results emphasized the coexistence and dichotomy of two well-defined tubule forms in both native and overexpressed cells, rather than continuously evolving tubule widths. Interestingly, different cell types were dominated by either of the two tubule forms, with the rat primary astrocytes and neurons being two contrasting cases dominated by the R2 and R1 forms, respectively. The latter finding echoes recent EM observations that the neuronal ER tubules are curiously thin at ∼20-nm diameter (36). Whereas STORM showed that the overexpression of Rtn4 and analogs drove ER tubules into the R1 form and that the entering of Climp63 into tubules produced the R2 form, immunoblotting (*SI Appendix*, Fig. S2) did not indicate the intracellular levels of Rtn4 or Climp63 to be the driving force behind the contrasting R1/R2 abundances between cell types. One worthy question is what drives Climp63 into the ER tubules versus confined localization to the ER sheets, for which multiple factors may be considered, including recent findings that Climp63 and other ER proteins differently interact with different microtubule populations (37).

Advances in electron tomography and focused ion beam scanning electron microscopy offer more holistic pictures of the ER structure. Examination of the resultant three-dimensional models identified tubules of elliptical cross-sections (13, 16, 17). In particular, one study has shown ribbon-like tubules in which immunogold-labeled Rtn4 appears to decorate the two high-curvature edges (16). These results are potentially consistent with our R2 tubule model. However, immunogold yields sparse labeling and does not readily accommodate multitarget imaging, and EM generally offers limited fields of view. STORM readily resolved Rtn4 (and analogs) throughout the cell to establish the R1–R2 dichotomy, and its multicolor capabilities further facilitated mechanistic investigations. The observed good correspondence of the Climp63-positive and -negative tubules to the R2 and R1 forms thus enabled us to employ multicolor live-cell imaging to unveil the rich second/subsecond dynamics of the two tubule forms as they differently accommodated luminal and membrane proteins.

Our results underscore how the intricate interactions between ER-shaping proteins give rise to molecularly related yet structurally and functionally distinct ER forms. Notably, in addition to identifying a conserved R2 tubule width across different cell types, we further established a positive correlation between this width and the Climp63 intraluminal size, thus emphasizing the coregulation of both the R1–R2 dichotomy and the final tubule geometry by Climp63 and membrane curvature-promoting proteins. How the Climp63–Rtn4 (and analog) interplays highlighted here further cooperate with other ER-shaping proteins, as well as how the R1 and R2 tubules, with their contrasting accommodation of luminal and membrane proteins, respectively participate in the diverse ER functions, present pressing questions for future experimental and theoretical efforts.

Materials and Methods

Plasmids. FLAG-Climp63, GFP-Climp63, GFP-Rtn3c(mouse), and HA tag (YPYDVPDYA)-REEP5(mouse) were gifts from Tom Rapoport, Harvard Medical School, Boston, MA (10, 11). Rtn4a-GFP (Addgene plasmid 61807) and mCherry-Climp63(mouse) (Addgene plasmid 136293) were gifts from Gia Voeltz, University of Colorado, Boulder, CO (38). mEmerald-sec61b (Addgene plasmid 54249), mEmerald-ER-3 (Addgene plasmid 54082), and calnexin-

mEmerald (Addgene plasmid 54021) were gifts from Michael Davidson, National High Magnetic Field Laboratory, Tallahassee, FL. The pcDNA3.1(+) backbone was prepared by digesting the pcDNA3.1(+) IRES GFP plasmid (Addgene plasmid 51406; a gift from Kathleen Collins, University of Michigan, Ann Arbor, MI) using the restriction enzymes *Eco*RI (ThermoFisher, FD0274) and *Xba*I (ThermoFisher, FD0684). Rtn4b-GFP was generated by inserting two PCR-amplified fragments from the initial part (RTN4 amino acid [AA] 1 to 185) and the later part (RTN4 AA 1005 to 1192 plus AcGFP1) of Rtn4a-GFP into the pcDNA3.1(+) backbone using Gibson Assembly (New England Biolabs, E2611S). Rtn4b-HaloTag was generated by inserting PCR-amplified Rtn4b from Rtn4b-GFP and PCR-amplified HaloTag from pSEMS-Tom20-HaloTag (Addgene plasmid 111135; a gift from Karin Busch, University of Münster, Münster, Germany) into the pcDNA3.1(+) backbone using Gibson Assembly. mCherry-Climp63(2xlumen) was prepared by assembling the full-length mCherry-Climp63(mouse) with the luminal part of mouse Climp63 (AA 110 to 575). The two fragments were both PCR-amplified from mCherry-Climp63(mouse) and assembled by Gibson Assembly onto the pcDNA3.1(+) backbone. The codons for the first five AAs of the second luminal domain were changed from ctGgaGgaGgtCcaG to ctAgaAgaAgtAcaA, which did not alter the encoded AAs (LEEVQ). mCherry-Climp63(1–192), mCherry-Climp63(1–301), mCherry-Climp63(1–336), and mCherry-Climp63 (1–437) were generated by inserting the PCR-amplified corresponding front parts of mCherry-Climp63(mouse) into the pcDNA3.1(+) backbone using Gibson Assembly. HaloTag-sec61b was prepared by inserting PCR-amplified HaloTag from pSEMS-Tom20-HaloTag and the sec61b fragment from mEmerald-sec61b into the pcDNA3.1(+) backbone using Gibson Assembly. HaloTag-ER-3 was generated by inserting PCR-amplified calreticulin signal peptide plus the three-AA linker from mEmerald-ER-3 and HaloTag from pSEMS-Tom20-HaloTag, plus a C-terminal KDEL ER retention signal included in the primer during the PCR amplification, into the pcDNA3.1(+) backbone. mEmerald (luminal)-canxTM was prepared by inserting the PCR-amplified calreticulin signal peptide, three-AA linker, mEmerald from mEmerald-ER-3, and the PCR-amplified calnexin transmembrane domain plus cytosolic residues (canxTM, AA 482 to 592 from human calnexin) from calnexin-mEmerald into the pcDNA3.1(+) backbone using Gibson Assembly. canxTM-mEmerald (cytosolic) was generated by inserting the PCR-amplified calnexin signal peptide plus a seven-AA linker from mEmerald-calnexin and the later part of calnexin-mEmerald (canxTM-14-AA linker-mEmerald) into the pcDNA3.1 backbone using Gibson Assembly. Rtn3c-mEmerald, REEP5-mEmerald, and Arl6IP1-mEmerald were generated by inserting PCR-amplified Rtn3c from GFP-Rtn3c(mouse), REEP5 from HA-REEP5(mouse), and Arl6IP1 from Myc-DDK-Arl6IP1 (OriGene, RC201681), respectively, and mEmerald from mEmerald-ER-3 into the pcDNA3.1(+) backbone using Gibson Assembly. Protein-coding sequences were verified by Sanger sequencing at the University of California (UC) Berkeley DNA Sequencing Facility.

Antibodies. Primary antibodies used are as follows: rabbit polyclonal anti-Rtn4a/b (ThermoFisher, PA1-41220), sheep polyclonal anti-Rtn4b (R&D Systems, AF6034), rabbit polyclonal anti-calreticulin (Abcam, ab2907), rabbit polyclonal anti-calnexin (ProteinTech, 10427-2-AP), rabbit monoclonal anti-sec61b (Cell Signaling Technology, 14648S), mouse monoclonal anti–α-tubulin (Sigma, T6199, DM1A), sheep polyclonal anti-Climp63 (R&D Systems, AF7355), mouse monoclonal anti-Climp63 (Enzo Life Sciences, ENZ-ABS669-0100, G1/296), mouse monoclonal anti-FLAG (Sigma-Aldrich, F1804, M2), mouse monoclonal anti-GFP (ThermoFisher, A11120), rabbit polyclonal anti-GFP (ThermoFisher, A11122), and Alexa Fluor 647–conjugated rabbit polyclonal anti-GFP (ThermoFisher, A31852). For both single-color and two-color STORM, Alexa Fluor 647–conjugated secondary antibodies (Invitrogen, goat anti-rabbit immunoglobulin G [IgG], A21245; donkey anti-sheep IgG, A21448) were used to label the target for imaging under 647-nm excitation. For two-color STORM, the second target was labeled by a secondary antibody (Jackson ImmunoResearch) conjugated with CF568 succinimidyl ester (Biotium, 92131) for imaging under 560-nm excitation.

Cell Culture and Transfection. COS-7, BSC-1, U2OS, A7r5, NIH 3T3, and C2C12 cells (UC Berkeley Cell Culture Facility) were maintained in Dulbecco's modified Eagle's media (DMEM) supplemented with 10% fetal bovine serum at 37 °C with 5% CO_2. Cells were cultured on no. 1.5 coverslips for 2 to ∼3 d until reaching ∼70% confluency. Rat astrocytes and neurons from embryonic day 18 hippocampus (BrainBits) were plated on poly-D-lysine–coated no. 1.5 coverslips. Astrocytes were cultured in the NbAstro medium (BrainBits). Neurons were cultured in the NbActiv1 medium (BrainBits) for ∼14 d. Plasmid transfection was performed using Lipofectamine 3000 (Invitrogen, L3000-008) according to the manufacturer's specifications, using ∼0.5 to 1 μg per well in 24-well plates (Corning, CLS3527) or Lab-Tek II chambered coverglass. Transfected cells were incubated for 1 to 2 d before subsequent experiments. Silencer Select siRNA against Climp63 (ThermoFisher, 4392420-s21594) and scrambled Silencer Select control siRNA (5′-GUACCAAUUCGUAAGUGUUTT-3′; 5′-AACACUUACGAAUUGGUACTT-3′) were transfected using Lipofectamine RNAiMAX (ThermoFisher, 13778100) according to the manufacturer's specifications. About 50 pmol siRNA was transfected into each well in 6-well plates. The siRNA-transfected cells were cultured for 3 d before subsequent experiments.

Immunoblotting. Suspensions of cultured cells were centrifuged at 4,200 rpm, resuspended, and washed with Dulbecco's phosphate-buffered saline (DPBS) twice before lysis. Cells were then lysed in a lysis buffer (150 mM NaCl, 50 mM Tris, 5 mM ethylenediaminetetraacetate, 1% Triton X, pH 7.5) at 4 °C for 30 min. Neurons were directly lysed in the cell-culture flask with the lysis buffer and then transferred to a microcentrifuge tube. Cell lysates were centrifuged for 20 min at 12,000 rpm. The supernatant was aspirated, and Halt Protease Inhibitor (ThermoFisher, 1862209) was added. Protein concentration was determined using the Pierce Rapid BCA Protein Assay Kit (ThermoFisher, A53226). Lithium dodecyl sulfate (1×) loading buffer (ThermoFisher, NP0007) and 70 mM dithiothreitol were added to a 20- to 30-μg protein sample. The sample was then incubated at 75 °C for 15 min. Electrophoresis was performed on a NuPAGE 4 to 12% or 10% Bis-Tris gel (Invitrogen, NP0302BOX and NP0315BOX) in 1× MOPS SDS Running Buffer (Invitrogen, NP0001) for ∼2 h at 90 V. The sample was then transferred to a methanol-activated polyvinylidene difluoride (PVDF) membrane (ThermoFisher, 22860) in the transfer buffer at 18 V for 50 min. The transfer buffer was prepared as 25 mM Tris (Acros Organics, 42457-1000), 192 mM glycine (Sigma-Aldrich, G8898), and 10% volume (vol)/vol methanol in water. The PVDF membrane was blocked with 5% bovine serum albumin (BSA; Sigma-Aldrich, A3059) or 5% nonfat dry milk (Cell Signaling Technology, 9999S) in TBST (20 mM Tris, 150 mM NaCl, 0.1% Tween 20, pH ∼7.5) for 30 min at room temperature (RT). The membrane was incubated with diluted primary antibodies in 5% BSA or 5% nonfat dry milk in TBST at 4 °C overnight and then washed three times with TBST buffer. The membrane was then incubated with the corresponding dye-conjugated secondary antibodies at RT for 1 h followed by three additional washes with TBST buffer. The membrane was then imaged with a GE Typhoon FLA 9500 variable mode laser scanner image analyzer.

Immunofluorescence. Cells were fixed with 3% (vol/vol) paraformaldehyde (Electron Microscopy Sciences, 15714) and 0.1% (vol/vol) glutaraldehyde (Electron Microscopy Sciences, 16365) in DPBS at RT for 20 min, and then washed twice with a freshly prepared 0.1% (weight [wt]/wt) $NaBH_4$ solution followed by three additional washes with DPBS. Samples were then blocked and permeabilized using a DPBS-based blocking buffer containing 0.1% (wt/wt) saponin (Sigma-Aldrich, S4521) and 5% (vol/vol) donkey serum (Jackson ImmunoResearch, 017000121) for sheep antibodies or 3% (wt/wt) BSA for other antibodies, for 30 min at RT. Samples were next incubated with diluted primary antibodies (1:200, sheep anti-Rtn4b; 1:100, rabbit anti-Rtn4a/b; 1:100, rabbit anti-calreticulin; 1:100, rabbit anti-calnexin; 1:100, rabbit anti-sec61b; 1:200, mouse anti-FLAG; 1:400, mouse anti-GFP; 1:200, rabbit anti-GFP) in the blocking buffer overnight at 4 °C. Samples were washed three times with washing buffer (0.1× blocking buffer diluted with DPBS) after primary labeling. Samples were then incubated with diluted dye-labeled secondary antibodies (1:400 for the commercial antibodies; 1:50 for the homemade antibodies) in the blocking buffer for 30 min at RT, followed by three additional washes with the washing buffer.

STORM SRM. STORM imaging was performed on a homebuilt inverted microscope using a Nikon CFI Plan Apo λ 100× oil-immersion objective (numerical aperture [NA] 1.45), as described previously (39, 40). The dye-labeled samples were mounted with a Tris·HCl–based imaging buffer containing 5% (wt/vol) glucose, 100 mM cysteamine (Sigma-Aldrich, 30070), 0.8 mg/mL glucose oxidase (Sigma-Aldrich, G2133), and 40 μg/mL catalase (Sigma-Aldrich, C30). Diffraction-limited wide-field images were first sequentially recorded for the different color channels using weak (∼50 mW/cm^2) laser excitations at 647 nm (for Alexa Fluor

647), 560 nm (for mCherry and CF568), and 488 nm (for GFP) using matching band-pass filters. For STORM imaging of targets labeled by Alexa Fluor 647 and CF568, the sample was sequentially imaged using strong 647- and 560-nm lasers at ∼2 kW/cm^2. The angle of incidence was slightly smaller than the critical angle of total internal reflection, thus illuminating a few micrometers into the sample. A weak (0 to 1 W/cm^2) 405-nm laser was applied to assist photoswitching. The resulting stochastic photoswitching of single-molecule fluorescence was recorded using an Andor iXon Ultra 897 EM-CCD (electron-multiplying charge-coupled device) camera at 110 frames per second (fps), for a total of ∼80,000 frames per image. The raw STORM data were analyzed according to previously described methods (28, 29, 41).

Live-Cell Fluorescence Microscopy. Cells were plated in Lab-Tek II chambered coverglass and transfected as described above. For imaging of HaloTag-labeled targets, 0.25 μM JF635 HaloTag ligand (a gift from Luke Lavis, Janelia Research Campus, Ashburn, VA) was added to the cell-culture medium for 30 min and then rinsed off with the imaging medium. The imaging medium was DMEM containing Hepes (ThermoFisher, 21063029). Live-cell fluorescence microscopy was performed on a Nikon Eclipse Ti-E inverted fluorescence microscope using a CFI Plan Apo λ 100× oil-immersion objective (NA 1.45) with an additional 1.5× magnification on the microscope body. A multi–band-pass filter cube (Semrock, Di01-R405/488/561/635 as the dichroic mirror; Chroma, ZET405/488/561/640m as the emission filter) was used. Two-color imaging of GFP and mCherry was achieved by alternating the excitation laser between 488 and 560 nm in successive frames as an Andor iXon Ultra 897 EM-CCD camera recorded at 4 fps, hence an effective time resolution of 0.5 s for two-color wide-field images. Three-color imaging of GFP, mCherry, and JF635 was achieved by alternating the excitation laser between 488, 560, and 647 nm in successive frames at camera frame rates of 4 or 3 fps, hence effective time resolutions of 0.75 or 1 s for three-color wide-field images.

Electron Microscopy. COS-7 cells grown on 35-mm MatTek glass-bottom dishes were fixed with 2% glutaraldehyde and 2% paraformaldehyde in PBS. The sample was rinsed in a 0.1 M sodium cacodylate buffer (pH 7.2), and immersed in 1% osmium tetroxide with 1.6% potassium ferricyanide in the same buffer for 30 min. The sample was rinsed and then subjected to an ascending ethanol gradient followed by pure ethanol. The sample was progressively infiltrated with Epon resin and polymerized at 60 °C. Thin (∼80-nm) sections were cut using a Leica UC6 ultramicrotome, and poststained with 2% uranyl acetate followed by Reynold's lead citrate. The sections were imaged using an FEI Tecnai 12 120-kV transmission electron microscope.

Data Availability. All study data are included in the article and/or supporting information.

ACKNOWLEDGMENTS. We thank Danielle Jorgens and Reena Zalpuri at the UC Berkeley Electron Microscope Laboratory for help with electron microscopy. We acknowledge support by the National Institute of General Medical Sciences of the NIH (DP2GM132681), Packard Fellowships for Science and Engineering, and Pew Charitable Trusts (to K.X.). K.X. is a Chan Zuckerberg Biohub Investigator.

1. A. R. English, G. K. Voeltz, Endoplasmic reticulum structure and interconnections with other organelles. *Cold Spring Harb. Perspect. Biol.* **5**, a013227 (2013).
2. U. Goyal, C. Blackstone, Untangling the web: Mechanisms underlying ER network formation. *Biochim. Biophys. Acta* **1833**, 2492–2498 (2013).
3. L. M. Westrate, J. E. Lee, W. A. Prinz, G. K. Voeltz, Form follows function: The importance of endoplasmic reticulum shape. *Annu. Rev. Biochem.* **84**, 791–811 (2015).
4. D. S. Schwarz, M. D. Blower, The endoplasmic reticulum: Structure, function and response to cellular signaling. *Cell. Mol. Life Sci.* **73**, 79–94 (2016).
5. H. Zhang, J. Hu, Shaping the endoplasmic reticulum into a social network. *Trends Cell Biol.* **26**, 934–943 (2016).
6. H. Wu, P. Carvalho, G. K. Voeltz, Here, there, and everywhere: The importance of ER membrane contact sites. *Science* **361**, eaan5835 (2018).
7. Y. Shibata, G. K. Voeltz, T. A. Rapoport, Rough sheets and smooth tubules. *Cell* **126**, 435–439 (2006).
8. Y. Shibata, J. Hu, M. M. Kozlov, T. A. Rapoport, Mechanisms shaping the membranes of cellular organelles. *Annu. Rev. Cell Dev. Biol.* **25**, 329–354 (2009).
9. G. K. Voeltz, W. A. Prinz, Y. Shibata, J. M. Rist, T. A. Rapoport, A class of membrane proteins shaping the tubular endoplasmic reticulum. *Cell* **124**, 573–586 (2006).
10. J. Hu *et al.*, Membrane proteins of the endoplasmic reticulum induce high-curvature tubules. *Science* **319**, 1247–1250 (2008).
11. Y. Shibata *et al.*, Mechanisms determining the morphology of the peripheral ER. *Cell* **143**, 774–788 (2010).
12. N. Zurek, L. Sparks, G. Voeltz, Reticulon short hairpin transmembrane domains are used to shape ER tubules. *Traffic* **12**, 28–41 (2011).
13. M. Puhka, M. Joensuu, H. Vihinen, I. Belevich, E. Jokitalo, Progressive sheet-to-tubule transformation is a general mechanism for endoplasmic reticulum partitioning in dividing mammalian cells. *Mol. Biol. Cell* **23**, 2424–2432 (2012).
14. T. Shemesh *et al.*, A model for the generation and interconversion of ER morphologies. *Proc. Natl. Acad. Sci. U.S.A.* **111**, E5243–E5251 (2014).
15. S. Wang, H. Tukachinsky, F. B. Romano, T. A. Rapoport, Cooperation of the ER-shaping proteins atlastin, lunapark, and reticulons to generate a tubular membrane network. *eLife* **5**, e18605 (2016).
16. O. Rämö *et al.*, NOGO-A/RTN4A and NOGO-B/RTN4B are simultaneously expressed in epithelial, fibroblast and neuronal cells and maintain ER morphology. *Sci. Rep.* **6**, 35969 (2016).
17. J. Nixon-Abell *et al.*, Increased spatiotemporal resolution reveals highly dynamic dense tubular matrices in the peripheral ER. *Science* **354**, aaf3928 (2016).
18. G. Gao, C. Zhu, E. Liu, I. R. Nabi, Reticulon and CLIMP-63 regulate nanodomain organization of peripheral ER tubules. *PLoS Biol.* **17**, e3000355 (2019).
19. L. K. Schroeder *et al.*, Dynamic nanoscale morphology of the ER surveyed by STED microscopy. *J. Cell Biol.* **218**, 83–96 (2019).
20. B. Shen *et al.*, Calumenin-1 interacts with Climp63 to cooperatively determine the luminal width and distribution of endoplasmic reticulum sheets. *iScience* **22**, 70–80 (2019).
21. N. Wang *et al.*, Mechanism of membrane-curvature generation by ER-tubule shaping proteins. *Nat. Commun.* **12**, 568 (2021).
22. P. A. Sandoz, F. G. van der Goot, How many lives does CLIMP-63 have? *Biochem. Soc. Trans.* **43**, 222–228 (2015).
23. K. Xu, G. Zhong, X. Zhuang, Actin, spectrin, and associated proteins form a periodic cytoskeletal structure in axons. *Science* **339**, 452–456 (2013).
24. S. J. Sahl, S. W. Hell, S. Jakobs, Fluorescence nanoscopy in cell biology. *Nat. Rev. Mol. Cell Biol.* **18**, 685–701 (2017).
25. Y. M. Sigal, R. Zhou, X. Zhuang, Visualizing and discovering cellular structures with super-resolution microscopy. *Science* **361**, 880–887 (2018).
26. S. H. Shim *et al.*, Super-resolution fluorescence imaging of organelles in live cells with photoswitchable membrane probes. *Proc. Natl. Acad. Sci. U.S.A.* **109**, 13978–13983 (2012).
27. F. Bottanelli *et al.*, Two-colour live-cell nanoscale imaging of intracellular targets. *Nat. Commun.* **7**, 10778 (2016).
28. M. J. Rust, M. Bates, X. Zhuang, Sub-diffraction-limit imaging by stochastic optical reconstruction microscopy (STORM). *Nat. Methods* **3**, 793–795 (2006).
29. M. Bates, B. Huang, G. T. Dempsey, X. Zhuang, Multicolor super-resolution imaging with photo-switchable fluorescent probes. *Science* **317**, 1749–1753 (2007).
30. M. Beck *et al.*, The quantitative proteome of a human cell line. *Mol. Syst. Biol.* **7**, 549 (2011).
31. A. Schweizer, J. Rohrer, J. W. Slot, H. J. Geuze, S. Kornfeld, Reassessment of the subcellular localization of p63. *J. Cell Sci.* **108**, 2477–2485 (1995).
32. J. D. Schrag *et al.*, The structure of calnexin, an ER chaperone involved in quality control of protein folding. *Mol. Cell* **8**, 633–644 (2001).
33. N. Tolley *et al.*, Overexpression of a plant reticulon remodels the lumen of the cortical endoplasmic reticulum but does not perturb protein transport. *Traffic* **9**, 94–102 (2008).
34. Y. S. Yang, N. Y. Harel, S. M. Strittmatter, Reticulon-4A (Nogo-A) redistributes protein disulfide isomerase to protect mice from SOD1-dependent amyotrophic lateral sclerosis. *J. Neurosci.* **29**, 13850–13859 (2009).
35. Y. Yamamoto, A. Yoshida, N. Miyazaki, K. Iwasaki, T. Sakisaka, Arl6IP1 has the ability to shape the mammalian ER membrane in a reticulon-like fashion. *Biochem. J.* **458**, 69–79 (2014).
36. M. Terasaki, Axonal endoplasmic reticulum is very narrow. *J. Cell Sci.* **131**, jcs210450 (2018).
37. P. Zheng *et al.*, ER proteins decipher the tubulin code to regulate organelle distribution. *Nature* **601**, 132–138 (2022).
38. Y. Shibata *et al.*, The reticulon and DP1/Yop1p proteins form immobile oligomers in the tubular endoplasmic reticulum. *J. Biol. Chem.* **283**, 18892–18904 (2008).
39. M. Wojcik, M. Hauser, W. Li, S. Moon, K. Xu, Graphene-enabled electron microscopy and correlated super-resolution microscopy of wet cells. *Nat. Commun.* **6**, 7384 (2015).
40. M. Zhang, S. J. Kenny, L. Ge, K. Xu, R. Schekman, Translocation of interleukin-1β into a vesicle intermediate in autophagy-mediated secretion. *eLife* **4**, e11205 (2015).
41. B. Huang, W. Wang, M. Bates, X. Zhuang, Three-dimensional super-resolution imaging by stochastic optical reconstruction microscopy. *Science* **319**, 810–813 (2008).